Check for updates

Design of Al-decorated $C_{24}N_{24}$ fullerene for efficient adsorption and removal of methylene blue dye from water

Habib Ullah, [ID] [a] Zakir Zaman Khan, [b] Akif Safeen, [c] Adnan Ali Khan, [ID] [d] Noor Ul Islam, [e] Ghafar Ali, [ID] [f] Basit Ali, [ID] *[g] Imran Shakir[h] and Yi Xie [ID] *[a]

In this study, density functional theory (DFT) is used to explore aluminum-doped porphyrin-like porous fullerene ($Al_6@C_{24}N_{24}$) as a potential adsorbent for scavenging aquatic carcinogenic methylene blue (MB) dye. The $Al_6@C_{24}N_{24}$ system demonstrates thermal stability up to 1000 K, implying the robust incorporation of Al atoms into the $C_{24}N_{24}$ framework. The adsorption analysis at the DFT-D3 level reveals that MB dye is efficiently adsorbed on the surface of the $Al_6@C_{24}N_{24}$ framework, with adsorption energies ranging from −2.03 to −2.97 eV. The charge-density-difference (CDD) mapping, partial-density of states (PDOS), and quantum theory of atoms-in-molecules (QTAIM) analyses validate the electrostatic interactions, facilitating MB chemisorption on the $Al_6@C_{24}N_{24}$ surface. The maximum uptake capacity assessment indicates that the $Al_6@C_{24}N_{24}$ system can effectively adsorb up to six MB molecules, highlighting its potential for efficient dye scavenging. Moreover, molecular dynamics (MD) simulations demonstrate the thermodynamically feasible formation of the $6MB\text{-}Al_6@C_{24}N_{24}$ complex at 300 K in an aqueous environment, substantiating the existence of the complex in real scenarios. These findings provide a theoretical basis for experimental investigations, suggesting that $Al_6@C_{24}N_{24}$ could serve as an innovative wastewater purifier by scavenging organic carcinogenic dyes, contributing to advancements in environmental remediation technologies.

1. Introduction

Methylene blue (MB) is a water-soluble phenothiazinium dye with a stable structure and a dark green appearance[1–3] that is commonly used for a spectrum of applications, both industrial and non-industrial, as a dyeing and colouring additive.[4–10] Apart from its applications, MB can cause adverse effects on human health, including neurotoxicity, hemolytic anemia, carcinogenicity, mutagenicity, cardiovascular, and reproductive effects, along with gastrointestinal and discoloration issues.[11–14] Due to its extensive use, MB often enters the natural aquatic ecosystem, posing a risk not only to human health but also to the overall environment.[3,15]

To address the challenges of removing such carcinogenic pollutants, several treatment methods, including membrane filtration and advanced oxidation processes, have been reported.[1–3,10] The effectiveness of these methods largely depends on the physicochemical characteristics of the micropollutants and specific operational parameters. Optimizing these variables is crucial for achieving efficient pollutant removal under diverse environmental conditions.[3] On the other hand, adsorption presents a straightforward and effective method for scavenging hazardous pollutants, including MB from wastewater.[16] Due to its uncomplicated design, low cost, resilience to various toxic substances, and operational simplicity, adsorption is often favoured over other wastewater treatment techniques.[17]

Numerous nanomaterials, such as graphene, graphene oxide, activated carbon, and various metals and metal oxides, have been investigated as adsorbents for the effective removal of dyes from wastewater, both experimentally and computationally.[18–22] Specifically, MB dye has been removed successfully from wastewater using activated carbon in experimental setups,[1,2,4,10,15,21,23] whereas metal oxides and other nanomaterial adsorbents have been reported in computational studies.[23–26] Despite these advancements, there remains

[a]*State Key Laboratory of Silicate Materials for Architectures, Wuhan University of Technology, Wuhan 430070, P.R. China. E-mail: xiey@whut.edu.cn*

[b]*Department of Chemistry, University of Malakand, Dir Lower, Chakdara, 18800, Khyber Pakhtunkhwa, Pakistan*

[c]*Department of Physics, University of Poonch Rawalakot, Rawalakot, 12350, Pakistan*

[d]*School of Science, Harbin Institute of Technology (Shenzhen), Shenzhen, China*

[e]*Department of Chemistry, Government Degree College Lalqilla Dir Lower, Lalqilla 18350, Khyber Pakhtunkhwa, Pakistan*

[f]*Nanomaterials Research Group (NRG), Physics Division, PINSTECH, Nilore, Islamabad, Pakistan*

[g]*Department of Chemistry and Materials Science, School of Chemical Engineering, Aalto University, P.O. Box 16100, FI-00076 Aalto, Finland. E-mail: basit.ali@aalto.fi*

[h]*Department of Physics, Faculty of Science, Islamic University of Madinah, Madinah 42351, Saudi Arabia*

a significant need to explore novel adsorbents that combine high porosity, excellent adsorption capacity, environmental safety, and cost-effectiveness. Moreover, gaining a deeper understanding of the adsorption mechanisms at the molecular level is essential for optimizing dye-removal processes.

In recent years, nitrogen-doped porous carbon-based nanomaterials have attracted considerable attention as emerging adsorbents due to their economical synthesis methods, large surface areas, and remarkable adsorption properties.[27–31] Considering the synthesis of these nanomaterials, reactive-magnetron sputtering and chemical-vapor deposition (CVD) are the most common methods for their fabrication.[32–34] Introducing nitrogen atoms into carbon-based structures, such as fullerenes, can alter the carbon π-electron system as a result of charge transfer between the nitrogen and carbon atoms. Consequently, the polar C–N bonds in nitrogen-doped carbon frameworks become preferred sites for nucleophilic or electrophilic interactions.[35] A novel form of porous fullerene, represented as $C_{24}N_{24}$, comprising eight triazine rings connected by C–C bonds, was theoretically proposed by Srinivasu and Ghosh, highlighting its potential as an advanced adsorbent material.[36] Furthermore, this innovative porous nanocluster (fullerene) is characterized by nitrogen-containing cavities similar in structure to those found in porphyrin molecules, with six such nitrogen sites present in $C_{24}N_{24}$ fullerene.[36] Studies have shown that when $C_{24}N_{24}$ fullerenes are doped with metals, such as lithium, aluminium, and various transition metals, they can serve as highly effective catalysts and hydrogen-storage materials.[36–38] Specifically, $C_{24}N_{24}$ fullerenes decorated with iron or silicon atoms have displayed remarkable catalytic performance, notably facilitating nitrogen oxide (NO) reduction and carbon monoxide (CO) oxidation reactions.[39–41]

Research indicates that N_4 cavities in $C_{24}N_{24}$ fullerenes serve as optimal sites for binding foreign atoms, such as metals and metalloids, through robust N–X covalent bonds (where X represents the metal or metalloid). This bonding minimizes the risk of atom clustering or aggregation on the fullerene surface, maintaining a stable distribution. In computational studies, achieving high chemical accuracy in predicting structural and electronic properties requires careful consideration of several factors, for instance, a large basis set, incorporation of relativistic effects, and accurate treatment of electronic correlations. When these conditions are fulfilled, simulations can yield precise insights into the material's properties.[42]

The present work investigates the adsorption of methylene blue (MB) dye on aluminium-decorated $C_{24}N_{24}$ fullerene ($Al_6@C_{24}N_{24}$), using first-principles simulations. The incorporation of an Al atom into the N_4 cavity of $C_{24}N_{24}$ significantly enhances its interaction with MB dye molecules. The observed high negative adsorption energies for MB molecules over the Al active sites on the surface of the $Al_6@C_{24}N_{24}$ adsorbent suggest their robust interaction. These computational findings indicate that $Al_6@C_{24}N_{24}$ holds great promise as an adsorbent material for scavenging toxic dyes from aqueous environments.

2. Computational details

In this study, spin-polarized density functional theory (DFT) implemented in the DMol^3 package was adopted for the overall simulations.[43,44] Structural optimizations and electronic property evaluations were carried out using the Perdew–Burke–Ernzerhof (PBE) exchange-correlation functional under the generalized-gradient approximation (GGA) framework,[45] along with the double-numerical-plus-polarization (DNP) basis set.[46] To ensure stability of the optimized structures, Hessian analyses were conducted at the same theoretical level and basis set, whereas the absence of negative vibrations confirmed structural stability. Key computational parameters included the basis set cutoff of 4.6 Å in addition to the thermal-smearing of 0.136 eV. Moreover, Grimme's DFT-D3 empirical method was applied to consider the van der Waals interactions.[47,48] Structural relaxations were performed with convergence thresholds of 0.027 eV Å^{-1} for force, 0.005 Å for maximum displacement, and 2.72 × 10^{-4} eV for energy.[49] Additionally, the implicit solvation effect was introduced using the conductor-like screening model (COSMO) with water as the solvent ($\varepsilon = 78.5$) to study the effect of solvation in an aqueous medium. The energy of adsorption (E_{ad}) of different complex structures was determined as:

$$E_{ad} = E_{complex} - (E_{adsorbent} + E_{adsorbate}) \tag{1}$$

where the terms $E_{complex}$, $E_{adsorbent}$, and $E_{adsorbate}$ refer to the ground-state optimized energies of MB-adsorbed $Al@C_{24}N_{24}$ (complex), Al-doped $C_{24}N_{24}$ (adsorbent), and the MB molecule (adsorbate), respectively. Additionally, the E_{ad} of Al atom incorporation into $C_{24}N_{24}$ was calculated to evaluate the stability of the Al-coordinated structure:

$$E_{ad} = E_{Al@C_{24}N_{24}} - (E_{C_{24}N_{24}} + E_{Al}) \tag{2}$$

Here, $E_{Al@C_{24}N_{24}}$ and $E_{C_{24}N_{24}}$ are the ground-state optimized energies of Al-incorporated and bare $C_{24}N_{24}$ nano-architecture, respectively, whereas E_{Al} denotes the isolated Al atom energy.

3. Results and discussion

3.1 Geometry, electronic properties, and stability of $Al@C_{24}N_{24}$

In our initial investigations, we examined the structural and electronic characteristics of both the bare and Al-decorated $C_{24}N_{24}$ nanocages, along with the MB dye molecule. The optimized geometries and electronic properties of the bare $C_{24}N_{24}$ nanocage and MB dye are presented in Fig. S1. As illustrated, the $C_{24}N_{24}$ nanocage (Fig. S1a) features highly electronegative N_4 cavities, resembling those in porphyrin structures, which have been identified as ideal sites for metal or metalloid anchoring in previous studies.[50–54] This fullerene comprises eight triazine rings that are interconnected by C–C bonds. Calculations indicate that the C–N and C–C bond distances are approximately 1.34 and 1.55 Å, respectively, which are consistent with the previous findings.[50,51,53,54] Additionally, the MEP map (Fig. S1c) elaborates the electronegative nature of the N_4

cavities, where the four electron-rich nitrogen atoms are shown by red spots (like corners) in the cavity. Earlier research has further confirmed that the N_4 cavity within the $C_{24}N_{24}$ framework is a preferred anchoring site for foreign atoms, such as silicon and aluminium.[54,55] Therefore, in this study, an aluminum atom was initially positioned within the N_4 cavity of a $C_{24}N_{24}$ nanocage, followed by full geometric relaxation.

Optimized configurations of $C_{24}N_{24}$ fullerenes incorporating a single Al atom and six Al atoms (Al@$C_{24}N_{24}$ and Al$_6$@$C_{24}N_{24}$), along with their corresponding partial density of states (PDOS) plots, can be viewed in Fig. 1 and S2 respectively. These post-optimized geometries revealed that the Al atom acquires the top-center position of the N_4 cavity plane, forming four equivalent Al–N bonds with nearby nitrogen atoms, each measuring approximately 1.87 Å. This bond length is marginally longer than that observed in Si@$C_{24}N_{24}$ (1.82 Å) and aligns closely with the previously reported value (1.87 Å) for Al@$C_{24}N_{24}$.[55,56] The N–Al–N bond angles are around 147.6°, indicating a slight deviation of the Al atom from the N_4 plane. The calculated E_{ad} value of Al on $C_{24}N_{24}$ is approximately −6.91 eV at the DFT-D3 level, indicating a strong interaction between the Al and the neighbouring nitrogen atoms, which would potentially inhibit the diffusion and clustering of Al atoms within the nanocage.[50,51,55,56] Similarly, Hirshfeld charge-transfer analysis suggests that almost 0.50 e is withdrawn by the adjacent nitrogen atoms from the centrosymmetric Al atom, conferring ionic character to the Al–N bond by the notably uneven charge distribution. Additionally, the PDOS analysis (Fig. S2c) reveals strong hybridization between the p-orbitals of the Al and N atoms at the Fermi level, further supporting the robust Al–N bond formation within the $C_{24}N_{24}$ structure.[57–59]

As indicated by the optimized geometry of pristine $C_{24}N_{24}$ fullerene (Fig. S1a), each N_4 cavity can serve as an excellent site for Al adsorption, as corroborated in reported studies.[56] Accordingly, this study explores the adsorption of Al atoms across all the N_4 cavities. The optimized geometry of the Al$_6$@$C_{24}N_{24}$ complex (Fig. 1) demonstrates that each Al atom is firmly captured within an N_4 cavity, adopting a tetragonal-pyramidal coordination with neighbouring nitrogen atoms, consistent with previous findings.[50,51,55,56] The Al–N bond lengths were calculated to be around 1.91 Å, which are slightly longer than those observed in single Al@$C_{24}N_{24}$. The average E_{ad} value of each Al atom was approximately −5.18 eV, suggesting a gradual decrease in affinity of the nanocage for Al adsorption as the number of adsorbed Al atoms increases. Moreover, the PDOS analysis (Fig. 1b) reveals an overlap between the p-orbitals of Al and N atoms below the Fermi level, indicating a slight weakening of the Al–N bonds with each additional Al atom. Furthermore, Hirshfeld charge analysis showed a decrease in the atomic charge of Al atoms to 0.54 e upon multiple Al adsorption in the fullerene, leading to an enhancement in the Lewis-acidic characteristics and subsequent surface reactivity of the Al@$C_{24}N_{24}$ nanomaterial.

Previous literature[60–62] highlighted the significant influence of surface-charge density distribution on the adsorption behaviour of MB molecules on nanomaterials. In this context, the MEP maps of Al$_6$@$C_{24}N_{24}$ and Al@$C_{24}N_{24}$ complexes are illustrated in Fig. S3a and S4b, respectively. As depicted in blue, the electron-depleted regions are prominent around the Al atoms, indicating the electropositive nature of Al atoms. Given the higher electronegativity difference between N and Al (3.04 vs. 1.61, based on the Pauling scale), the N atoms exhibit a more nucleophilic character in comparison to the electrophilic nature of the Al atom within the Al$_6$@$C_{24}N_{24}$ nanostructure. Likewise, the charge-density difference (CDD) (Fig. S3b) and deformation-charge density (DCD) (Fig. S3c) analyses support these findings, showing a notable electron density reduction on the Al atom, further affirming its electropositive character. This suggests that Al atoms are capable of forming electrostatic interactions with the negatively charged fullerene adsorbate.

The quantum theory of atoms-in-molecules (QTAIM) analysis is usually performed to characterize the nature of a chemical bond through AIM parameters, such as the electron density $\rho(r)$, the Laplacian of electron density $\nabla^2\rho(r)$, and the total energy density $H(r)$. According to QTAIM theory, if $\nabla^2\rho(r) < 0$ and $H(r) < 0$ at a given bond critical point (BCP), the bond would be
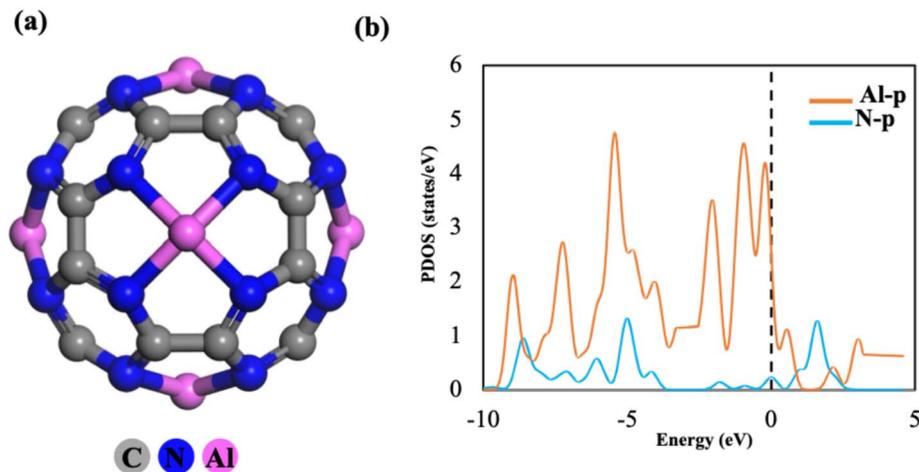

Fig. 1 Optimized geometry of six Al-incorporated $C_{24}N_{24}$ fullerene (Al$_6$@$C_{24}N_{24}$) (a) and its corresponding partial density of states plot (b).

a shared shell (covalent) interaction. However, if both $\nabla^2\rho(r)$ and $H(r)$ are positive (>0), the interaction would be a closed shell (purely electrostatic, noncovalent or weak H-bond) interaction. Alternatively, the interaction would be a polar covalent or a strong H-bond if $\nabla^2\rho(r) > 0$ and $H(r) < 0$.[63,64] The molecular graphs of $Al_6@C24N_{24}$ and $Al@C_{24}N_{24}$ complexes are displayed in Fig. S3d and S5, respectively, whereas the QTAIM parameters are listed in Table S1. According to the above criteria, the Al–N bonding within the $C_{24}N_{24}$ framework is primarily governed by polar covalent interactions, since $\nabla^2\rho(r)$ values are positive and $H(r)$ values are negative. An analogous idea regarding the electrostatic nature of the Al–N bond is provided by the CDD and DCD maps in Fig. S3b and c), which further infer the stability and integrity of the $Al_6@C_{24}N_{24}$ complex. In addition, the HOMO–LUMO energy gap for $Al_6@C_{24}N_{24}$ was calculated to be 0.97 eV (Fig. S3e and f), highlighting the electronic characteristics of the system.

To evaluate the thermal stability of the $Al_6@C_{24}N_{24}$ system, *ab initio* molecular dynamics (AIMD) simulations were conducted. These simulations were performed at temperatures of 500 and 1000 K over a period of 2 ps and 10 ps. The final geometries obtained from the AIMD simulations are presented in Fig. 7a and b and S6. Remarkably, $Al_6@C_{24}N_{24}$ maintained its structural integrity at both temperatures, with all the Al atoms maintaining their positions above the N_4 cavities. Yet, minor fluctuations in the Al–N bond distances were observed, suggesting the strong polar covalent nature of the bond between the Al and N atoms. Based on these findings, we propose that the $Al_6@C_{24}N_{24}$ system exhibits high thermal stability, remaining structurally resilient at temperatures up to 1000 K.

3.2 Application of $Al@C_{24}N_{24}$ as an adsorbent for MB removal

To explore the MB dye adsorption efficiency of the $Al@C_{24}N_{24}$ complex as an adsorbent for scavenging carcinogenic dyes from water, we examined the adsorption characteristics of the MB dye on the original $C_{24}N_{24}$ surface, as investigated earlier.[65] The optimized structure of the $MB@C_{24}N_{24}$ complex, along with its corresponding CDD and PDOS plots, is shown in Fig. S8a and c. Key parameters, including bond lengths, E_{ad} value, and charge transfer, are presented in Table S3, which are in agreement with previously reported data.[65] From the geometry relaxation analysis, it is observed that the MB molecule binds to the surface of bare $C_{24}N_{24}$ fullerene *via* two H⋯N intermolecular bonds, measuring between 2.38 and 2.42 Å, indicating a physisorption interaction. The calculated E_{ad} value of this complex is −0.49 eV. Hirshfeld charge-transfer analysis reveals a minimal uptake of charges by hydrogen atoms of the MB from the $C_{24}N_{24}$ surface. This idea is further verified by CDD analysis, as depicted in Fig. S8b, which shows no significant electron-density overlap between the N and H atoms of the $C_{24}N_{24}$ nanocage and the MB dye, respectively. Analogously, PDOS analysis (Fig. S8c) further supports the above-mentioned findings; here, the absence of electronic-states coupling around the Fermi level between the $C_{24}N_{24}$ fullerene and MB signifies a physical interaction rather than chemical bonding. To further

verify these physical interactions, we conducted AIM analysis. Fig. S9 displays the molecular graph, while Table S3 summarizes the AIM parameters. The very small values of $\rho(r)$ (0.008 a.u.) and the positive values of $\nabla^2\rho(r)$ and $H(r)$, reveal the existence of weak hydrogen bonds (H⋯N) and van der Waals forces between the MB dye and the $C_{24}N_{24}$ surface,[61,62] indicating the dye molecule is only loosely adsorbed onto the pristine $C_{24}N_{24}$ system.

To enhance the adsorption capability of the $C_{24}N_{24}$ system for scavenging MB dye from water, the system is modified by incorporating Al atoms. Fig. 2 illustrates the different possible interactions of MB dye with the Al-decorated $C_{24}N_{24}$ fullerene. Based on the MEP map of the MB (Fig. S1d), the nitrogen (N1) atom, present in the central ring, is recognised as the most nucleophilic site, carrying −0.185 e charge density. Consequently, the N1 atom of MB is chosen for the interaction with the Al atom of the $Al@C_{24}N_{24}$ system. Furthermore, sulphur (S) in the central ring and the nitrogen (N2) atom in the $H_3C–N–CH_3$ moieties at the edges of the MB molecule are also considered for the interaction with the Al atom. In the first adsorption configuration (configuration-1), given in Fig. 2a, the MB dye is positioned in such a way that the N1 atom faces the Al atom of the $Al@C_{24}N_{24}$ system. After structural optimization, it is observed that the N1 atom forms a strong covalent bond with the Al atom, with a bond distance of 1.89 Å. Likewise, intermolecular hydrogen bonding (H⋯N) occurs between the dye and the N atoms of the $Al@C_{24}N_{24}$ system, with a bond distance of 2.50 Å. These interactions result in a high E_{ad} value of −2.97 eV at the DFT-D3 level, as summarized in Table 1. Hirshfeld charge analysis reveals a reduction in the positive charge of the Al atom from 0.507 to 0.399 e, indicating a charge transfer of −0.109 e from MB to the adsorbent. In the second adsorption configuration (configuration-2), shown in Fig. 2b, the MB molecule is aligned above the $Al@C_{24}N_{24}$ in such a way that the S atom of the central ring of MB interacts with the Al atom of the adsorbent. After structural relaxation, a S–Al covalent bond, with a length of 2.37 Å, is observed, which is deemed responsible for the adsorption of MB over the fullerene surface at the cost of −2.08 eV as E_{ad}, as shown in Table 1. Hirshfeld analysis indicates a charge transfer of −0.149 e from the S atom of the dye to the Al atom. In the third adsorption configuration (configuration-3), presented in Fig. 2c, the MB dye interacts *via* the N2 atom of the $H_3C–N–CH_3$ group. Geometry optimization shows the formation of an Al–N bond with a bond distance of 2.0 Å. Additionally, two weak hydrogen bonds are observed, with bond lengths of 2.74 Å and 2.52 Å. The E_{ad} value for this configuration (N2 site) is determined to be −2.18 eV, indicating stronger adsorption than the S-site interaction but weaker than the N1-site interaction. Charge-transfer analysis reveals that −0.113 e is shifted from the MB molecule to the adsorbent. To confirm the feasibility of the adsorption process, we also calculated the Gibbs' free energy change (ΔG) from the frequency calculations for all the complexes by including the entropy effect and ZPTE corrections. The ΔG values, given in Table 1, are all negative, confirming the exothermic nature and feasibility of the adsorption process under normal conditions.[66,67]
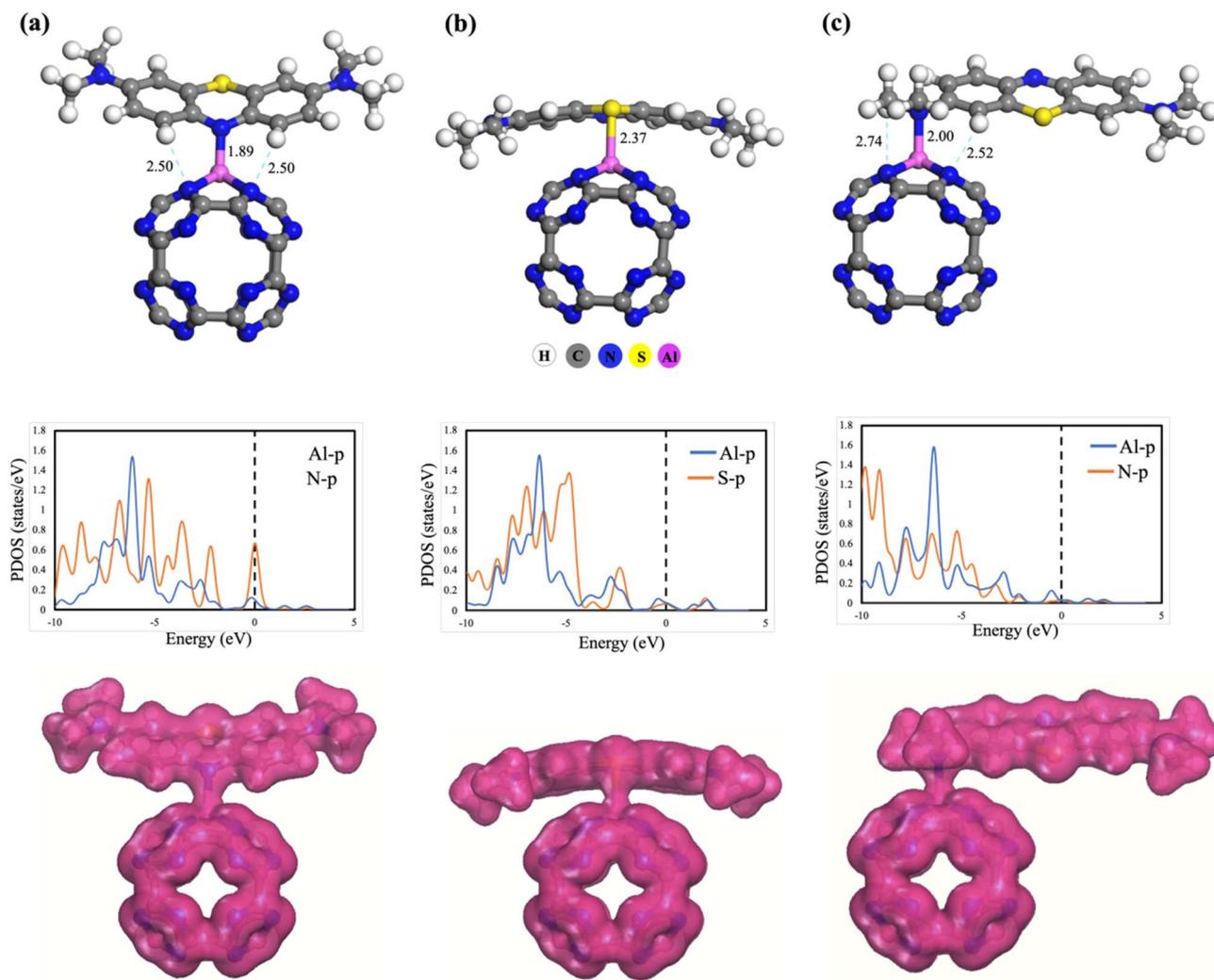
Fig. 2 The optimized geometries of Al@$C_{24}N_{24}$ complexes with MB adsorption *via* the N(1) site (a), the S site (b), and the N(2) site (c), and their corresponding partial density of states and charge density difference plot. All distances are in Å.

To gain deeper insights into the chemisorption mechanism of MB on the Al@$C_{24}N_{24}$ system, electronic structure analyses, including PDOS, CDD, and AIM were performed for the optimized adsorption configurations. The PDOS plots (Fig. 2) reveal a considerable overlap at the Fermi level between the p-orbitals of Al and the p-orbitals of N or S atoms of the dye. This overlap indicates the formation of a strong interaction and suggests chemisorption of the MB dye molecule over the surface of the Al@$C_{24}N_{24}$ system. The CDD plots for the adsorption of the MB molecule over the Al@$C_{24}N_{24}$ system (Fig. 2) demonstrate

substantial electron-density redistribution at the interface for all configurations. This redistribution proves the strong interaction between the dye and the adsorbent surface, supporting the chemisorption mechanism. AIM analysis further confirms these findings, with the molecular graphs showing the three interactions of MB with Al@$C_{24}N_{24}$ visualized in Fig. 3. In the AIM analysis for configuration-1 (Fig. 3a), the values of $\rho(r)$, $\nabla^2\rho(r)$, and $H(r)$ (Table 1) were calculated to be 0.076, 0.445, and −0.0045 a.u., respectively, for the N–Al bond. The high values of $\rho(r)$ and $\nabla^2\rho(r)$, along with the negative $H(r)$ value, support the

Table 1 Calculated bond distance (Å), adsorption energy (E_{ad} eV), dispersion-corrected adsorption energy (E_{ad-D3} eV), charge transfer (Q_{CT} e), Gibbs free energy change (ΔG eV), electron density ($\rho(r)$ a.u), Laplacian of the electron density ($\nabla^2\rho(r)$ a.u), and energy density ($H(r)$ a.u.) for MB molecule adsorption over the Al@$C_{24}N_{24}$ complex

Complex	X–Al (X = N, S)	E_{ad}	E_{ad-D3}	ΔG	Q_{CT}	$\rho(r)$	$\nabla^2\rho(r)$	$H(r)$
MB-Al@$C_{24}N_{24}$-N(1)	1.89, 2.50, 2.50	−3.07	−2.97	−2.43	−0.109	0.076 (Al–N), 0.012 (H⋯N)	0.445 (Al–N), 0.038 (H⋯N)	−0.0045, 0.0011
MB-Al@$C_{24}N_{24}$-S	2.37	−2.13	−2.03	−1.83	−0.149	0.049 (Al–S)	0.129 (Al–S)	−0.0012
MB-Al@$C_{24}N_{24}$-N(2)	2.00, 2.74, 2.52	−2.31	−2.18	−1.97	−0.113	0.061 (Al–N), 0.011 (H⋯N)	0.307 (Al–N), 0.036 (H⋯N)	−0.0040, 0.0011

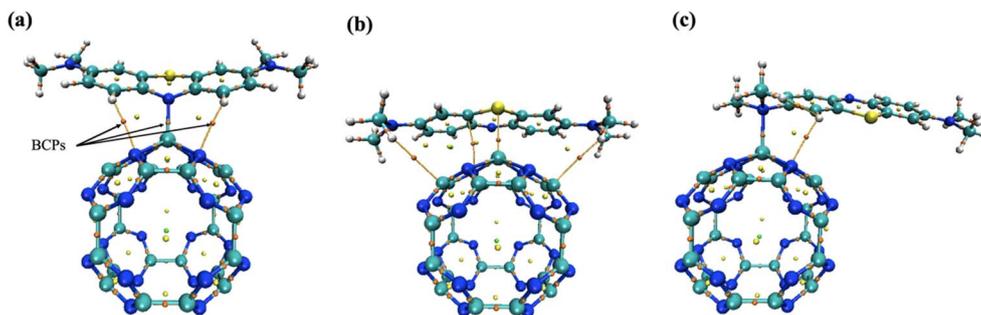**Fig. 3** AIM molecular graphs of the MB-adsorbed Al@$C_{24}N_{24}$ complex involving the N(1) site (a), the S site (b), and the N(2) site (c). BCPs show bond critical points.

strong polar covalent interaction of the MB dye molecule with the surface of the Al@$C_{24}N_{24}$.[61,62] The Al–S bond in adsorption configuration-2 (Fig. 3b) shows lower values of $\rho(r)$ (0.049), $\nabla^2\rho(r)$ (0.129), and $H(r)$ (−0.012 a.u), signifying a moderate interaction with partial covalent character. Similarly, for adsorption configuration-3 (Fig. 3c), the N–Al bond exhibits $\rho(r)$, $\nabla^2\rho(r)$, and $H(r)$ values of 0.06, 0.307, and −0.0040 a.u., respectively, implying a weaker electrostatic interaction with a covalent nature. Additionally, the idea of hydrogen bonds (N–H) being involved in configurations-1 and configurations-3, while van der Waals interactions being involved in configuration-2, has been suggested based on AIM analysis. Consequently, the AIM data provide strong evidence regarding the chemisorption of MB over the Al@$C_{24}N_{24}$ system, which results from the collective effects of covalent bonds, hydrogen bonds, and other intermolecular interactions.

To evaluate the maximum dye-uptake capability of the fullerene as an adsorbent, multiple MB molecules were interacted with the fully functionalized Al$_6$@$C_{24}N_{24}$ fullerene and examined. The optimized geometry of six MB molecules simultaneously adsorbed over the surface of Al$_6$@$C_{24}N_{24}$ in the form of a complex (represented as 6MB-Al$_6$@$C_{24}N_{24}$) and the corresponding CDD plot, are displayed in Fig. 4a and b, respectively. As observed in the single MB adsorption study, the central (N1) atom of the MB molecule that was identified as the most feasible site of attachment was also considered for the interactions in the multi-adsorption configuration. After

geometry relaxation, the MB molecules were found to adsorb strongly onto the Al$_6$@$C_{24}N_{24}$ surface, with an average Al–N bond length of 1.87 Å in the 6MB-Al$_6$@$C_{24}N_{24}$. This short bond distance indicates robust interactions between the dye and the adsorbent, signifying strong adsorption behavior. The adsorption energy per MB molecule for 6MB-Al$_6$@$C_{24}N_{24}$ complex was found to be −3.05 eV. This highly negative value is indicative of chemisorption of the dye over the adsorbent surface. Hirshfeld charge analysis reveals an average charge transfer of −0.121 e from each MB molecule to the corresponding Al atom. This significant charge transfer facilitates the formation of strong Al–N1 covalent bonds, giving rise to effective MB adsorption over the Al$_6$@$C_{24}N_{24}$ surface. The CDD plots further support this finding, showing substantial electron-density overlap between the MB molecules and the Al$_6$@$C_{24}N_{24}$ system (Fig. 4b), which reinforces the chemisorption mechanism. These results demonstrate the exceptional adsorption capacity of the Al@$C_{24}N_{24}$ system, accommodating multiple MB molecules without any structural distortion. This study highlights the potential applications of Al$_6$@$C_{24}N_{24}$ as an efficient and robust adsorbent for dye removal applications.

To check the effect of solvation (hydration) on the adsorption of MB dye on Al@$C_{24}N_{24}$ adsorbent, the aqueous-phase solvation energy (E_{solv}) was calculated, and the results were correlated with the gaseous-phase calculations. The aqueous-phase E_{ad} values and charge transfer (given in Table 2) were also investigated during MB interaction with the Al@$C_{24}N_{24}$ adsorbent to better understand the impact of solvation. Table 2 shows that the aqueous-phase E_{ad} values are lower (less negative) than the gas-phase adsorption values, yet they are still negative. The lower aqueous-phase E_{ad} values suggest that the MB adsorption over the Al@$C_{24}N_{24}$ adsorbent is weakened by the aqueous medium due to the solvation effect and the polar

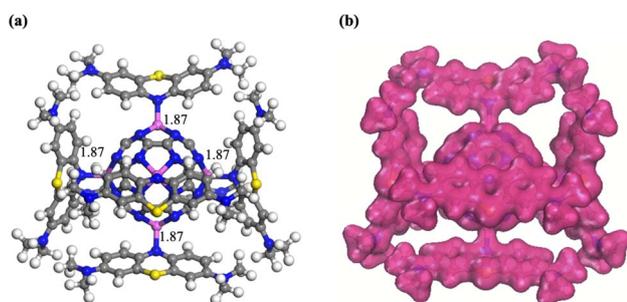**Fig. 4** The optimized geometry of the 6MB-adsorbed Al$_6$@$C_{24}N_{24}$ complex (a) and the corresponding charge density difference plot (b). All bond lengths are in Å.

Table 2 Computed adsorption energy (E_{ad} eV) and (Q_{CT} e) for MB adsorption over the Al@$C_{24}N_{24}$ system in the aqueous phase

Complex	E_{solv}	E_{solv-D_3}	$E_{ad\ (aq)}$	E_{ad-D_3}	Q_{CT}
MB-Al@$C_{24}N_{24}$-N(1)	−3.11	−2.88	−2.53	−2.44	−0.081
MB-Al@$C_{24}N_{24}$-S	−2.21	−2.13	−1.67	−1.52	−0.082
MB-Al@$C_{24}N_{24}$-N(2)	−2.37	−2.25	−1.81	−1.69	−0.069

nature of MB. However, the thermodynamic feasibility and stabilization of the MB-Al@$C_{24}N_{24}$ complex are further supported by the negative E_{solv} values (Table 2), calculated for all three adsorption configurations of the MB dye over the adsorbent. Furthermore, as evident from the Hirshfeld charge analysis, charge transfer from MB to Al@$C_{24}N_{24}$ is also reduced in an aqueous environment relative to the gaseous phase. It is concluded that releasing the MB molecule from the Al@$C_{24}N_{24}$ adsorbent is energetically more favorable in aqueous medium relative to the gaseous phase, highlighting the potential effects of solubility on desorption in practical applications.

To evaluate the selectivity of the Al@$C_{24}N_{24}$ adsorbent, the interaction of MB with the adsorbent in the presence of competitive ions, including OH^-, Na^+, Ca^{2+}, Cl^-, SO_4^{2-}, and H_2O molecules, was simulated. The optimized geometries of these interacting species, together with the adsorbent, are displayed in Fig. 5, and their binding energies are tabulated in Table S4. The binding energies obtained for these competitive ions, except OH^-, suggest that their presence would not hinder the MB adsorption over the Al@$C_{24}N_{24}$ adsorbent. Conversely, the OH^- ion exhibited strong binding ($E_{ad} = -5.05$ eV), probably due to its high charge density and strong basicity, allowing it to form a robust coordination with the electron-deficient Al site and likely obstructing MB access. Thus, it is inferred that the decontamination of MB from wastewater should be performed under neutral conditions, where the undesirable interaction is avoided due to the minimal OH^- ion concentration. However, although OH^- can bind strongly to the Al site, its

realistic interference in a slightly alkaline medium is reduced by the adsorption kinetics of MB, driven by π–π stacking, electrostatic attraction, and the potential Al–N coordination, owing to the larger molecular size and multidentate nature of MB relative to OH^-. The specificity of Al@$C_{24}N_{24}$ toward the MB dye over the OH^- ion is confirmed by the coadsorption complex (Fig. S10), obtained by placing a MB molecule near the Al active site of the adsorbent, where the OH^- ion is already bonded, followed by geometry optimization. The optimized coadsorption complex shows that the N site of the MB is attached to the Al active site by pushing the OH group a little outward. The adsorption energy calculated for this system is −1.98 eV, which indicates that the adsorbent can also adsorb MB in an alkaline medium. In addition, to further examine the selectivity of Al@$C_{24}N_{24}$ for MB, we examined the competitive adsorption of Rhodamine B (RB) dye over the adsorbent. The optimized geometry of adsorbed Rhodamine B dye over the adsorbent (RB-Al@$C_{24}N_{24}$) is illustrated in Fig. S11. The intermolecular bonding parameters and adsorption energy (Table S4) clearly indicate that the RB adsorption over Al@$C_{24}N_{24}$ is weak compared to MB. This proves that Al@$C_{24}N_{24}$ exhibits high selectivity toward MB over RB and other common ions in aqueous environments, confirming its potential application for practical wastewater treatment (Table 3 and S4).

In an acidic environment, MB can convert into its reduced form, leuco-methylene blue (LMB),[81] as depicted in Fig. 6. To investigate the adsorption characteristics of MB in such a medium, we examined the adsorption of LMB on the
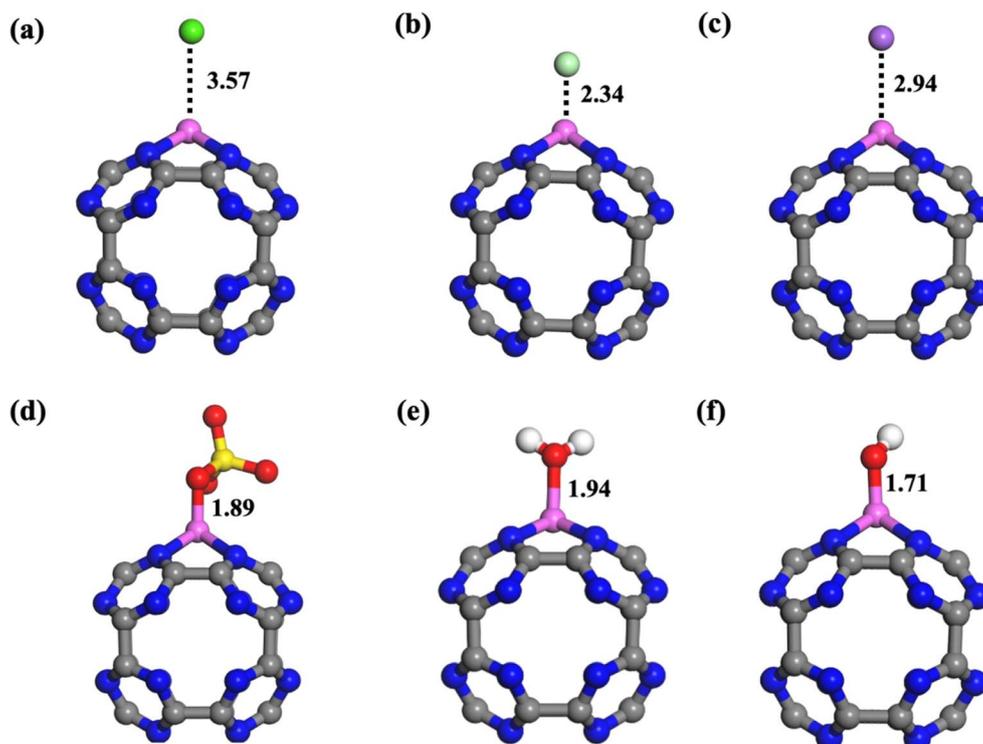

Fig. 5 Optimized geometries of Ca^{2+} (a), Cl^- (b), Na^+ (c), SO_4^{2-} (d), H_2O (e), and OH^- (f) adsorption over the Al@$C_{24}N_{24}$ adsorbent. All bond lengths are in Å.

Table 3 Comparative analysis of MB adsorption over different adsorbents

| Adsorbent	Capacity (mg g⁻¹)	No. of MB adsorbed	E_{ad} (eV)	Computational/experimental	ref.
Graphene oxide	—	1	−2.25	Computational and experimental	68
Cd or ZnCd/TiO₂	—	1	−1.15 or −1.127	Computational and experimental	69
Brazilian berries seed	188.26	1	−1.78	Computational and experimental	21
Alginic acid	51.34	1	−0.27	Computational and experimental	23
ZnTiO₃(101)	—	1	−1.31	Computational	24
TiO₂ (101)	—	1	−0.12	Computational	24
Polysaccharide-based composite hydrogel	122.1	—	—	Experimental	70
Hydrolyzed polyacrylamide	37.12	—	—	Experimental	71
Tectona grandis sawdust	172.41	—	—	Experimental	72
Cotton stalk	222.22	—	—	Experimental	73
Cellulosic olive stones biomass	88.2	—	—	Experimental	74
Walnut shell-carbon	315.00	—	—	Experimental	75
Oil palm shell-carbon	243.90	—	—	Experimental	76
Rice husk activated carbon	312	—	—	Experimental	77
Co/Ni-borophene	—	1	−2.99, −2.27	Computational	
G/C/dicyclohexyl, G/C/dimethylaminopropyl hydrochloride groups	274, 320	—	—	Experimental	78
TNTs/LDHs/OS	357	—	—	Experimental	79
SA/CMC-K composite microbeads	84.63	—	—	Experimental	80
Al₆@C₂₄N₂₄	ᵃ2441	6	−3.05	Computational	This study

ᵃ Theoretical capacity (mg g⁻¹).
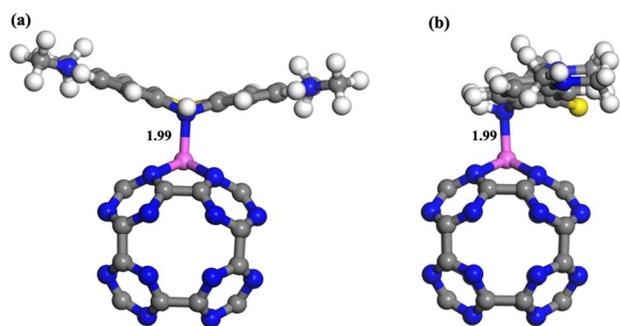
Fig. 6 Relaxed structures of the LMB adsorption over the Al@C₂₄N₂₄ from the front view (a) and the side view (b). All bond lengths are in Å.

Al@C₂₄N₂₄ adsorbent. The optimized structure of LMB on Al@C₂₄N₂₄ is illustrated in Fig. 6. LMB is firmly adsorbed onto the Al-decorated C₂₄N₂₄ with a binding distance of 1.99 Å. The adsorption energy value for this complex is −2.06 eV, which indicates that the Al-decorated C₂₄N₂₄ system can effectively adsorb dye molecules in an acidic medium.

To assess the stability and experimental feasibility of the 6MB-Al₆@C₂₄N₂₄ complex in a bulk aquatic environment, we applied the Amorphous Cell through Monte Carlo simulations with Adsorption Locator and Forcite code,[82] implemented in the Material Studio Package. For this purpose, the DFT-optimized 6MB-Al₆@C₂₄N₂₄ complex was initially enclosed inside a shell of around 80 water molecules in the amorphous cell, mimicking the bulk water system. The complex was initially optimized *via* the Amorphous Cell code, followed by full optimization through Forcite code using the COMPASS-III forcefield.[82] During this

optimization, 30 000 steps were set in the program, and the method of steepest descent was set in the minimizer.

The red spots in Fig. 7a, being observed in the cell through Adsorption Locator analysis, predict the most probable interactive sites for water molecules with the complex. These interactive sites are exactly confirmed by the Forcite optimization (Fig. 7b), where water molecules can be seen around the complex at the positions of the red spots. The relaxed geometry in Fig. 7b shows that no distortion or bond dangling is observed and that the intermolecular bond distances are consistent with those obtained from DFT analysis, which reflects the stability of the complex in the aqueous environment. However, the stability of a singly adsorbed MB molecule over the adsorbent (MB-Al@C₂₄N₂₄) has been predicted by the negative E_{solv} value (Table 2). The stable existence of the complex in water further validates that the adsorbent can easily adsorb the dye molecules in an
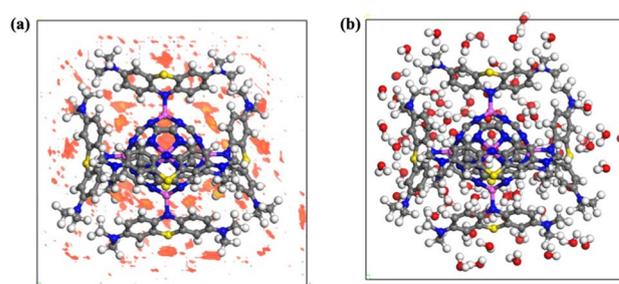

Fig. 7 Representation of possible water interaction sites (a) and the optimized geometry of the 6MB-Al₆@C₂₄N₂₄ in the amorphous cell containing 80 water molecules (b).

aquatic environment. Furthermore, these findings suggest that the results of the Forcite analysis are in close agreement with those of the Adsorption Locator analysis. The total electronic energy obtained *via* the COMPASS-III forcefield for the bulk structure is -5211.24 kcal mol^{-1}. The negative electronic energy value suggests the thermodynamically stable nature of the complex in bulk water.

To further check the thermal stability of the 6MB-Al$_6$@C$_{24}$N$_{24}$ complex in the bulk aquatic environment, we performed AIMD simulations *via* the Forcite code of the Amorphous Cell, with the complex surrounded by 80 water molecules, for a time period of 20 and 80 ps, with 1 and 2 fs at 300 K, respectively. The geometry after AIMD analysis and the potential energy fluctuation plots are presented in Fig. 8a and b; water molecules are excluded for simplicity to clearly visualize the intermolecular bonding sites between the dye and the adsorbent. The simulations show that the complex is highly stable (negligible intermolecular bond variations are observed) in the bulk environment; even when the temperature of the water is increased, the adsorbent can still stably adsorb the dye molecules from water.

The interaction of the adsorbate and adsorbent is of utmost significance in the adsorption phenomenon. Nonetheless, the recovery of adsorbents *via* desorption of adsorbates is the essence of an effective adsorption, which cannot be overlooked. As mentioned, the E_{ad} values for MB adsorption over Al@C$_{24}$N$_{24}$ by the three configurations (Fig. 2) were -2.97, -2.18, and -2.08 eV, respectively. These values reflect the irreversible adsorption of MB molecules over the surface of Al@C$_{24}$N$_{24}$, where the desorption does not occur unless special conditions are applied. At higher temperatures, the bond between MB and the adsorbent surface is likely to

weaken due to entropic effects, which generally facilitates the recyclability of the adsorbate. To quantitatively assess this, the desorption time (τ) of the adsorbed MB was calculated using the following relation:[83]

$$\tau = \nu^{-1} \, \exp\left(\frac{E_{ads}}{k_B T}\right) \tag{3}$$

In this context, T denotes the ambient temperature, which is 298.15, 398.15 and 498.15 K, while k_B is Boltzmann's constant, and ν is the attempt frequency, set at 10^{12} Hz. This formula indicates that the desorption time is exponentially related to E_{ad}, suggesting that even slight changes in binding strength can result in significant variations in desorption behavior. The predicted τ values (Table S5) for MB desorption from the Al@C$_{24}$N$_{24}$ surface are 1.63×10^{38}, 2.03×10^{21}, and 7.40×10^{24} s at 298.15 K, which decrease considerably as the temperature increases. It is worth mentioning that the calculated τ values correspond to idealized gas-phase interactions, obtained from DFT calculations. As observed from the solvent effect, the adsorption energies are observed to decrease (less negative) in aqueous medium. The decrease in interactive forces of the adsorbate–adsorbent complex is probably due to solvation effects, competitive water molecules' interactions with the adsorbent, and entropic contributions, which facilitate desorption by reducing the desorption barrier. Thus, it has been suggested that increasing the temperature of the aqueous medium would accelerate desorption of MB from the adsorbent in practice, ensuring regeneration of the adsorbent. Therefore, the adsorbent surface not only offers selective and stable adsorption of MB molecules but also facilitates their efficient desorption, a feature that is highly advantageous for practical pollutant sensing applications.
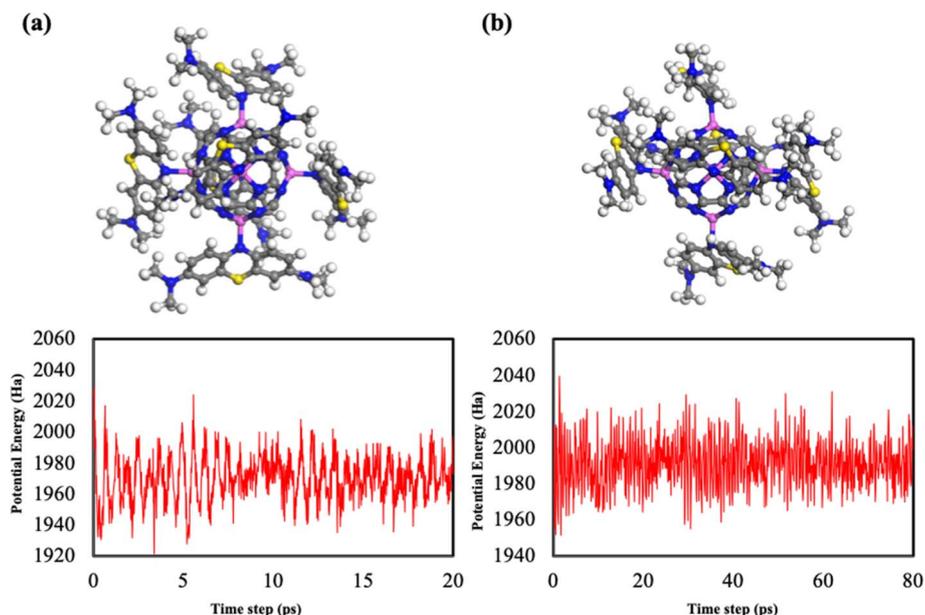

Fig. 8 Molecular structure of the 6MB–Al$_6$@C$_{24}$N$_{24}$ complex and its corresponding potential energy fluctuation plots after molecular dynamics simulations at 300 K for 20 ps with 1 fs (a) and 80 ps with 2 fs (b).

4 Conclusion

In this study, the potential applications of the Al@C$_{24}$N$_{24}$ complex as an adsorbent for scavenging carcinogenic MB dye from wastewater were investigated by DFT calculations. The results reveal that Al atoms strongly adhere to the C$_{24}$N$_{24}$ fullerene with high E_{ad} values of -6.91 and -5.18 eV at the DFT-D3 level, with the incorporation of single and multiple (six) Al atoms, respectively. Electronic properties analysis underscores Al sites on the C$_{24}$N$_{24}$ fullerene as the primary reactive sites for the adsorption of MB molecules. Similarly, structural information and AIM analysis indicate that MB is physisorbed over the pristine C$_{24}$N$_{24}$ system with an E_{ad} value of -0.49 eV. In contrast, MB molecules are chemisorbed over the Al@C$_{24}$N$_{24}$ surface *via* N1, S, and N2 sites, with significantly shorter bond lengths (*e.g.*, 1.89, 2.37, and 2.00 Å). These observed shorter distances are indicative of strong chemisorption, accompanied by higher E_{ad} values of -2.97, -2.08, and -2.18 eV at the DFT-D3 level. Moreover, the CDD, PDOS, and AIM analyses confirm that the interaction between the MB molecule and the Al@C$_{24}$N$_{24}$ surface is governed by covalent and hydrogen bonding. The adsorption capacity assessment reveals that Al-decorated C$_{24}$N$_{24}$ can accommodate up to six MB molecules, highlighting its high dye-uptake potential. Additionally, the solvation effect is deduced to facilitate the desorption of MB molecules from the surface of the Al@C$_{24}$N$_{24}$. To further check the solvation effect, we also performed simulations for the 6MB-Al$_6$@C$_{24}$N$_{24}$ complex in an aqueous environment by placing the complex in an amorphous cell with 80 water molecules. The geometry optimization and thermal stability study at 300 K show that the complex is highly stable in aqueous medium. This study represents the first demonstration of how Al incorporation significantly enhances the performance of C$_{24}$N$_{24}$ fullerene for MB removal from wastewater, providing insights into developing effective carcinogen scavengers for water purification.

Author contributions

Habib Ullah: conceptualization, software, validation and writing – original draft. Zakir Zaman Khan: validation, writing, review and editing. Akif Safeen: formal analysis and editing original draft. Adnan Ali Khan: computational tools, writing, review and editing. Noor Ul Islam: data curation, review and editing. Ghafar Ali: investigation, writing, review & editing. Basit Ali: funding acquisition, writing, review & editing the manuscript with helpful input and insight. Imran Shakir: formal analysis, review and editing. Xie Yi: supervision, project administration, writing, review and editing.

Conflicts of interest

The authors declare that they have no known competing financial interests or personal relationships that could have appeared to influence the work reported in this paper.

Data availability

The data supporting this article have been included as part of the supplementary information file (SI). Supplementary information is available. See DOI: https://doi.org/10.1039/d6ra00172f.

References

1 P. O. Oladoye, T. O. Ajiboye, E. O. Omotola and O. J. Oyewola, Methylene Blue Dye: Toxicity and Potential Elimination Technology from Wastewater, *Results Eng.*, 2022, **16**, 100678, DOI: 10.1016/j.rineng.2022.100678.

2 P. M. Thabede, N. D. Shooto and E. B. Naidoo, Removal of Methylene Blue Dye and Lead Ions from Aqueous Solution Using Activated Carbon from Black Cumin Seeds, *S. Afr. J. Chem. Eng.*, 2020, **33**, 39–50, DOI: 10.1016/j.sajce.2020.04.002.

3 M. Alshabib, M. A. Oluwadamilare, A. Tanimu, I. Abdulazeez, K. Alhooshani and S. A. Ganiyu, Experimental and DFT Investigation of Ceria-Nanocomposite Decorated AC Derived from Groundnut Shell for Efficient Removal of Methylene-Blue from Wastewater Effluent, *Appl. Surf. Sci.*, 2021, **536**, 147749, DOI: 10.1016/j.apsusc.2020.147749.

4 E. Farjami, L. Clima, K. V. Gothelf and E. E. Ferapontova, DNA Interactions with a Methylene Blue Redox Indicator Depend on the DNA Length and Are Sequence Specific, *Analyst*, 2010, **135**(6), 1443–1448, DOI: 10.1039/c0an00049c.

5 J. M. Small and H. Hintelmann, Methylene Blue Derivatization then LC-MS Analysis for Measurement of Trace Levels of Sulfide in Aquatic Samples, *Anal. Bioanal. Chem.*, 2007, **387**, 2881–2886, DOI: 10.1007/s00216-007-1140-3.

6 A. Richards, H. Marshall and A. McQuary, Evaluation of Methylene Blue, Thiamine, and/or Albumin in the Prevention of Ifosfamide-Related Neurotoxicity, *J. Oncol. Pharm. Pract.*, 2011, **17**(2), 109–114, DOI: 10.1177/1078155210385159.

7 B. Coulibaly, A. Zoungrana, F. P. Mockenhaupt, R. H. Schirmer, C. Klose, U. Mansmann, P. E. Meissner and O. Müller, Strong Gametocytocidal Effect of Methylene Blue-Based Combination Therapy against Falciparum Malaria: A Randomised Controlled Trial, *PLoS One*, 2009, **4**(5), e5318, DOI: 10.1371/journal.pone.0005318.

8 J. C. Y. Lo, M. A. Darracq and R. F. Clark, A Review of Methylene Blue Treatment for Cardiovascular Collapse, *J. Emerg. Med.*, 2014, **46**(5), 660–668, DOI: 10.1016/j.jemermed.2013.08.102.

9 I. A. W. Tan, B. H. Hameed and A. L. Ahmad, Equilibrium and Kinetic Studies on Basic Dye Adsorption by Oil Palm Fibre Activated Carbon, *Chem. Eng. J.*, 2007, **127**(1–3), 111–119, DOI: 10.1016/j.cej.2006.09.010.

10 A. M. M. Vargas, A. L. Cazetta, M. H. Kunita, T. L. Silva and V. C. Almeida, Adsorption of Methylene Blue on Activated Carbon Produced from Flamboyant Pods (Delonix regia): Study of Adsorption Isotherms and Kinetic Models, *Chem. Eng. J.*, 2011, **200–202**, 174–181, DOI: 10.1016/j.cej.2011.01.067.

11 C. C. Coddington, T. L. Anderson, C. R. Accetta, J. Swanson, T. Kruger and G. D. Hodgen, Adverse Effects of Methylene Blue on Human Sperm Motility, Components of Human Reproductive Tract Fluids, and Mouse Embryo Cleavage, *Fertil. Steril.*, 1989, **51**(3), 480–485, DOI: 10.1016/S0015-0282(16)60558-7.

12 S. J. Martindale and J. C. Stedeford, Neurological Sequelae Following Methylene Blue Injection for Parathyroidectomy, *Anaesthesia*, 2003, **58**(10), 1041–1042, DOI: 10.1046/j.1365-2044.2003.03415_23.x.

13 National Toxicology Program, Toxicology and Carcinogenesis Studies of Methylene Blue Trihydrate (CAS No. 7220-79-3) in F344/N Rats and B6C3F1 Mice (Gavage Studies), *Natl. Toxicol. Program Tech. Rep. Ser.*, 2008, **540**, 1–224.

14 L. Vutskits, A. Briner, P. Klauser, E. Gascon, A. G. Dayer, J. Z. Kiss, D. Muller, M. J. Licker and D. R. Morel, Adverse Effects of Methylene Blue on the Central Nervous System, *Anesthesiology*, 2008, **108**(4), 684–692, DOI: 10.1097/aln.0b013e3181684be4.

15 M. Ghaedi, A. G. Nasab, S. Khodadoust, R. Sahraei and A. Daneshfar, Characterization of Zinc Oxide Nanorods Loaded on Activated Carbon as Cheap and Efficient Adsorbent for Removal of Methylene Blue, *J. Ind. Eng. Chem.*, 2014, **20**(6), 4291–4299, DOI: 10.1016/j.jiec.2014.05.006.

16 O. Pezoti, A. L. Cazetta, I. P. A. F. Souza, K. C. Bedin, A. C. Martins, T. L. Silva and V. C. Almeida, Adsorption Studies of Methylene Blue onto ZnCl2-Activated Carbon Produced from Buriti Shells (Mauritia flexuosa L.), *J. Ind. Eng. Chem.*, 2014, **20**(5), 3698–3707, DOI: 10.1016/j.jiec.2014.02.007.

17 R. S. Raveendra, P. A. Prashanth, R. H. Krishna, N. P. Bhagya, B. M. Nagabhushana, H. R. Naika, K. Lingaraju, H. Nagabhushana and B. D. S. Prasad, Structural Characterization of Nano ZnTiO3 Ceramic: An Effective Azo Dye Adsorbent and Antibacterial Agent, *J. Asian Ceram. Soc.*, 2014, **2**(4), 352–359, DOI: 10.1016/j.jascer.2014.07.008.

18 M. Khan, M. Ikram, A. Haider, A. Ul-Hamid, H. Ullah, I. Shahzadi, S. Khan, M. B. Kanoun, S. Goumri-Said, F. Medina and W. Nabgan, Experimental and DFT Study of GO-Decorated CaO Quantum Dots for Catalytic Dye Degradation and Bactericidal Potential, *Front. Environ. Sci.*, 2023, **11**, 1158399, DOI: 10.3389/fenvs.2023.1158399.

19 G. Z. Kyzas, E. A. Deliyanni, D. N. Bikiaris and A. C. Mitropoulos, Graphene Composites as Dye Adsorbents: Review, *Chem. Eng. Res. Des.*, 2018, **130**, 26–44, DOI: 10.1016/j.cherd.2017.11.006.

20 M. S. Sadek, G. E. Khedr, M. F. A. Messih and M. A. H. Ismail, Experimental and DFT Study of Photocatalytic Activity of Reduced Graphene Oxide/Copper Sulfide Composite for Removal of Organic Dyes from Water, *Sci. Rep.*, 2023, **13**, 15435, DOI: 10.1038/s41598-023-42680-3.

21 A. Molla, Y. Li, B. Mandal, S. G. Kang, S. H. Hur and J. S. Chung, Selective Adsorption of Organic Dyes on Graphene Oxide: Theoretical and Experimental Analysis, *Appl. Surf. Sci.*, 2019, **465**, 1052–1061, DOI: 10.1016/j.apsusc.2018.09.056.

22 B. Mao, B. Sidhureddy, A. R. Thiruppathi, P. C. Wood and A. Chen, Efficient Dye Removal and Separation Based on Graphene Oxide Nanomaterials, *New J. Chem.*, 2020, **44**(15), 6049–6062, DOI: 10.1039/c9nj05895h.

23 L. Sellaoui, D. Franco, H. Ghalla, J. Georgin, M. S. Netto, G. L. Dotto, A. Bonilla-Petriciolet, H. Belmabrouk and A. Bajahzar, Insights of the Adsorption Mechanism of Methylene Blue on Brazilian Berries Seeds: Experiments, Phenomenological Modelling and DFT Calculations, *Chem. Eng. J.*, 2020, **394**, 125011, DOI: 10.1016/j.cej.2020.125011.

24 X. Jaramillo-Fierro, L. F. Capa, F. Medina and S. González, DFT Study of Methylene Blue Adsorption on ZnTiO3 and TiO2 Surfaces (101), *Molecules*, 2021, **26**(13), 3780, DOI: 10.3390/molecules26133780.

25 A. Allangawi, M. A. A. Aljar, K. Ayub, A. A. El-Fattah and T. Mahmood, Removal of Methylene Blue by Using Sodium Alginate-Based Hydrogel; Validation of Experimental Findings via DFT Calculations, *J. Mol. Graph. Model.*, 2023, **121**, 108468, DOI: 10.1016/j.jmgm.2023.108468.

26 H. Ouachtak, A. El Guerdaoui, R. El Haouti, R. Haounati, H. Ighnih, Y. Toubi, F. Alakhras, R. Rehman, N. Hafid, A. A. Addi and M. L. Taha, Combined Molecular Dynamics Simulations and Experimental Studies of the Removal of Cationic Dyes on the Eco-Friendly Adsorbent of Activated Carbon Decorated Montmorillonite Mt@AC, *RSC Adv.*, 2023, **13**, 5641–5657, DOI: 10.1039/d2ra08059a.

27 F. Gao, G. L. Zhao, S. Yang and J. J. Spivey, Nitrogen-Doped Fullerene as a Potential Catalyst for Hydrogen Fuel Cells, *J. Am. Chem. Soc.*, 2013, **135**(9), 3315–3318, DOI: 10.1021/ja311089a.

28 I. H. Lin, Y. H. Lu and H. T. Chen, Nitrogen-Doped C60 as a Robust Catalyst for CO Oxidation, *J. Comput. Chem.*, 2017, **38**(23), 2041–2046, DOI: 10.1002/jcc.24865.

29 S. H. Noh, C. Kwon, J. Hwang, T. Ohsaka, B. J. Kim, T. Y. Kim, Y. G. Yoon, Z. Chen, M. H. Seo and B. Han, Self-Assembled Nitrogen-Doped Fullerenes and Their Catalysis for Fuel Cell and Rechargeable Metal-Air Battery Applications, *Nanoscale*, 2017, **9**(21), 7373–7379, DOI: 10.1039/C7NR01232A.

30 X. Chen, J. Chang and Q. Ke, Probing the Activity of Pure and N-Doped Fullerenes Towards Oxygen Reduction Reaction by Density Functional Theory, *Carbon*, 2018, **126**, 53–57, DOI: 10.1016/j.carbon.2017.09.073.

31 A. A. Khan, I. Ahmad and R. Ahmad, Influence of Electric Field on CO2 Removal by P-Doped C60-Fullerene: A DFT Study, *Chem. Phys. Lett.*, 2020, **742**, 137155, DOI: 10.1016/j.cplett.2020.137155.

32 Z. C. Ying, R. L. Hettich, R. N. Compton and R. E. Haufler, Synthesis of Nitrogen-Doped Fullerenes by Laser Ablation, *J. Phys. B: At. Mol. Opt. Phys.*, 1996, **29**(21), 4935–4942, DOI: 10.1088/0953-4075/29/21/014.

33 L. Hultman, S. Stafström, Z. Czigány, J. Neidhardt, N. Hellgren, I. F. Brunell, K. Suenaga and C. Colliex, Cross-Linked Nano-Onions of Carbon Nitride in the Solid Phase: Existence of a Novel C48N12 Aza-Fullerene, *Phys. Rev. Lett.*, 2001, **87**(22), 225503, DOI: 10.1103/PhysRevLett.87.225503.

34 G. Otero, G. Biddau, C. Sánchez-Sánchez, R. Caillard, M. F. López, C. Rogero, F. J. Palomares, N. Cabello, M. A. Basanta, J. Ortega, J. Méndez, A. M. Echavarren, R. Pérez, B. Gómez-Lor and J. A. Martín-Gago, Fullerenes from Aromatic Precursors by Surface-Catalysed Cyclodehydrogenation, *Nature*, 2008, **454**(7205), 865–868, DOI: 10.1038/nature07160.

35 H. Sharma, I. Garg, K. Dharamvir and V. K. Jindal, Structural, Electronic, and Vibrational Properties of C60-nNn (n = 1–12), *J. Phys. Chem. A*, 2009, **113**(34), 9002–9013, DOI: 10.1021/jp903520w.

36 K. Srinivasu and S. K. Ghosh, Transition Metal Decorated Porphyrin-Like Porous Fullerene: Promising Materials for Molecular Hydrogen Adsorption, *J. Phys. Chem. C*, 2012, **116**(47), 25184–25189, DOI: 10.1021/jp308644w.

37 B. Modak, K. Srinivasu and S. K. Ghosh, Exploring Metal Decorated Porphyrin-Like Porous Fullerene as Catalyst for Oxygen Reduction Reaction: A DFT Study, *Int. J. Hydrogen Energy*, 2017, **42**(4), 2278–2287, DOI: 10.1016/j.ijhydene.2016.10.109.

38 M. D. Esrafili and B. Nejadebrahimi, N2O Reduction over a Porous Si-Decorated Carbon Nitride Fullerene: A DFT Study, *Chem. Phys. Lett.*, 2019, **716**, 11–16, DOI: 10.1016/j.cplett.2018.11.041.

39 H. Hamadi, E. Shakerzadeh and M. D. Esrafili, A DFT Study on the Potential Application of Si@C24N24 Porous Fullerene as an Innovative and Highly Active Catalyst for NO Reduction, *Chem. Phys. Lett.*, 2019, **724**, 104–110, DOI: 10.1016/j.cplett.2019.03.057.

40 M. D. Esrafili and H. Hamadi, Catalytic Oxidation of CO Using a Silicon-Coordinated Carbon Nitride Fullerene, *Mol. Phys.*, 2020, **118**(19), e1797919, DOI: 10.1080/00268976.2020.1797919.

41 E. Shakerzadeh, H. Hamadi and M. D. Esrafili, Computational Mechanistic Insights into CO Oxidation Reaction over Fe Decorated C24N24 Fullerene, *Inorg. Chem. Commun.*, 2019, **106**, 112–117, DOI: 10.1016/j.inoche.2019.06.014.

42 C. G. Zhan, Development and Application of First-Principles Electronic Structure Approach for Molecules in Solution Based on Fully Polarizable Continuum Model, *Acta Phys.-Chim. Sin.*, 2011, **27**(1), 1–12, DOI: 10.3866/PKU.WHXB20110101.

43 B. Delley, An All-Electron Numerical Method for Solving the Local Density Functional for Polyatomic Molecules, *J. Chem. Phys.*, 1990, **92**(1), 508–517, DOI: 10.1063/1.458452.

44 B. Delley, From Molecules to Solids with the DMol3 Approach, *J. Chem. Phys.*, 2000, **113**(18), 7756–7764, DOI: 10.1063/1.1316015.

45 J. P. Perdew, K. Burke and M. Ernzerhof, Generalized Gradient Approximation Made Simple, *Phys. Rev. Lett.*, 1996, **77**(18), 3865–3868, DOI: 10.1103/PhysRevLett.77.3865.

46 P. Liu and J. A. Rodriguez, Catalysts for Hydrogen Evolution from the [NiFe] Hydrogenase to the Ni2P(001) Surface: The Importance of Ensemble Effect, *J. Am. Chem. Soc.*, 2005, **127**(42), 14871–14878, DOI: 10.1021/ja0534135.

47 S. Grimme, Accurate Description of van der Waals Complexes by Density Functional Theory Including Empirical Corrections, *J. Comput. Chem.*, 2004, **25**(12), 1463–1473, DOI: 10.1002/jcc.20078.

48 S. Grimme, Semiempirical GGA-Type Density Functional Constructed with a Long-Range Dispersion Correction, *J. Comput. Chem.*, 2006, **27**(15), 1787–1799, DOI: 10.1002/jcc.20495.

49 V. A. Basiuk, O. V. Prezhdo and E. V. Basiuk, Thermal Smearing in DFT Calculations: How Small Is Really Small? A Case of La and Lu Atoms Adsorbed on Graphene, *Mater. Today Commun.*, 2020, **25**, 101595, DOI: 10.1016/j.mtcomm.2020.101595.

50 B. Modak, K. Srinivasu and S. K. Ghosh, Exploring Metal Decorated Porphyrin-Like Porous Fullerene as Catalyst for Oxygen Reduction Reaction: A DFT Study, *Int. J. Hydrogen Energy*, 2017, **42**(4), 2278–2287, DOI: 10.1016/j.ijhydene.2016.10.109.

51 K. Srinivasu and S. K. Ghosh, Transition Metal Decorated Porphyrin-Like Porous Fullerene: Promising Materials for Molecular Hydrogen Adsorption, *J. Phys. Chem. C*, 2012, **116**(47), 25184–25189, DOI: 10.1021/jp308644w.

52 M. D. Esrafili, Ca Functionalized N-Doped Porphyrin-Like Porous C60 as an Efficient Material for Storage of Molecular Hydrogen, *J. Mol. Model.*, 2021, **27**, 352, DOI: 10.1007/s00894-021-05015-5.

53 M. D. Esrafili and S. Hosseini, Reversible CO2 Storage and Efficient Separation Using Ca Decorated Porphyrin-Like Porous C24N24 Fullerene: A DFT Study, *RSC Adv.*, 2021, **11**, 33341–33349, DOI: 10.1039/d1ra05888f.

54 M. D. Esrafili and P. Mousavian, Sc-Functionalized Porphyrin-Like Porous Fullerene for CO2 Storage and Separation: A First-Principles Evaluation, *J. Mol. Graph. Model.*, 2021, **107**, 108112, DOI: 10.1016/j.jmgm.2021.108112.

55 M. D. Esrafili and P. Mousavian, Efficient Hydrogen Storage on Al Decorated C24N24: A DFT Study, *New J. Chem.*, 2021, **45**(42), 19442–19449, DOI: 10.1039/d1nj04096k.

56 A. H. Ragab, L. O. Mallasiy, S. R. AL-Mhyawi and I. Khan, Cooperative Six-Molecule N2O Splitting: Computational Exploration of 6Al@C24N24 as a High-Capacity Greenhouse Gas Catalyst, *Diam. Relat. Mater.*, 2026, **161**, 113073, DOI: 10.1016/j.diamond.2025.113073.

57 M. D. Esrafili, Electric Field Assisted Activation of CO2 over P-Doped Graphene: A DFT Study, *J. Mol. Graph. Model.*, 2019, **90**, 192–198, DOI: 10.1016/j.jmgm.2019.06.005.

58 M. D. Esrafili and S. Asadollahi, A Single Pd Atom Stabilized on Boron-Vacancy of h-BN Nanosheet: A Promising Catalyst for CO Oxidation, *ChemistrySelect*, 2018, **3**(32), 9181–9188, DOI: 10.1002/slct.201801622.

59 Z. Bai, X. Z. Jiang and K. H. Luo, Theoretical Exploration on the Performance of Single and Dual-Atom Cu Catalysts on the CO2 Electroreduction Process: A DFT Study, *Phys. Chem. Chem. Phys.*, 2023, **25**(34), 23717–23727, DOI: 10.1039/D3CP02591A.

60 M. D. Esrafili, A. A. Khan and P. Mousavian, Synergic Effects between Boron and Nitrogen Atoms in BN-Codoped C59–nBNn Fullerenes (n = 1–3) for Metal-Free Reduction of Greenhouse N2O Gas, *RSC Adv.*, 2021, **11**, 24821–24829, DOI: 10.1039/d1ra04046d.

61 Z. Liang, C. Liu, M. Chen, X. . ; U. . , P. K. Qi, S. G. Peera, J. Liu, J. He and T. Liang, Oxygen Reduction Reaction Mechanism on P, N Co-Doped Graphene: A Density Functional Theory Study, *New J. Chem.*, 2020, **44**(1), 248–257, DOI: 10.1039/c9nj04808a.

62 S. Sadeghi and M. Amani, Co-Doped Triel–Pnicogen Graphene as Metal-Free Catalyst for CO Oxidation: Role of Multi-Center Covalency, *J. Mol. Model.*, 2019, **25**, 85, DOI: 10.1007/s00894-019-3960-4.

63 N. S. Venkataramanan, A. Suvitha, R. Sahara and Y. Kawazoe, A Computational Study on the Complexation of Bisbenzimidazolyl Derivatives with Cucurbituril and Cyclohexylcucurbituril, *J. Inclusion Phenom. Macrocyclic Chem.*, 2021, **100**, 217–231, DOI: 10.1007/s10847-021-01078-8.

64 P. S. V. Kumar, V. Raghavendra and V. Subramanian, Bader's Theory of Atoms in Molecules (AIM) and Its Applications to Chemical Bonding, *J. Chem. Sci.*, 2016, **128**, 1527–1536, DOI: 10.1007/s12039-016-1173-4.

65 M. Alomar and A. A. Khan, Porphyrin Like Porous Fullerene Functionalized with Ga as an Effective Adsorbent for the Removal of Methylene Blue from Wastewater Effluent, *Surf. Interfaces*, 2024, **52**, 104883, DOI: 10.1016/j.surfin.2024.104883.

66 Z. Ali, R. Ahmad, W. A. Farooq, A. Khan, A. A. Khan, S. Bibi, B. Adalat, M. A. Almutairi, N. Yaqub and M. Atif, Synthesis and Characterization of Functionalized Nanosilica for Zinc Ion Mitigation; Experimental and Computational Investigations, *Molecules*, 2020, **25**(23), 5534, DOI: 10.3390/molecules25235534.

67 R. Ahmad, Z. Ali, A. A. Khan and N. U. Rehman, Terbium Extraction by Functionalized Surface: Experimental and DFT Approach, *Adsorption*, 2020, **26**, 117–125, DOI: 10.1007/s10450-019-00165-7.

68 Y. Li, Q. Du, T. Liu, J. Sun, Y. Wang, S. Wu, Z. Wang, Y. Xia and L. Xia, Methylene Blue Adsorption on Graphene Oxide/Calcium Alginate Composites, *Carbohydr. Polym.*, 2013, **95**(1), 164–171, DOI: 10.1016/j.carbpol.2013.01.094.

69 S. Khan, M. Sadiq and N. Muhammad, Enhanced Photocatalytic Potential of TiO2 Nanoparticles in Coupled CdTiO2 and ZnCdTiO2 Nanocomposites, *Environ. Sci. Pollut. Res.*, 2022, **29**, 47831–47845, DOI: 10.1007/s11356-022-19807-6.

70 R. Sivakumar and N. Y. Lee, Adsorptive Removal of Organic Pollutant Methylene Blue Using Polysaccharide-Based Composite Hydrogels, *Chemosphere*, 2022, **286**, 131890, DOI: 10.1016/j.chemosphere.2021.131890.

71 T. Ma, Y. Wu, N. Liu and Y. Wu, Hydrolyzed Polyacrylamide Modified Diatomite Waste as a Novel Adsorbent for Organic Dye Removal: Adsorption Performance and Mechanism Studies, *Polyhedron*, 2020, **175**, 114227, DOI: 10.1016/j.poly.2019.114227.

72 F. Mashkoor and A. Nasar, Magnetized Tectona grandis Sawdust as a Novel Adsorbent: Preparation, Characterization, and Utilization for the Removal of Methylene Blue from Aqueous Solution, *Cellulose*, 2020, **27**, 2613–2635, DOI: 10.1007/s10570-020-03000-2.

73 H. Deng, J. Lu, G. Li, G. Zhang and X. Wang, Adsorption of Methylene Blue on Adsorbent Materials Produced from Cotton Stalk, *Chem. Eng. J.*, 2011, **172**(1), 326–334, DOI: 10.1016/j.cej.2011.05.062.

74 M. A. Al-Ghouti and R. S. Al-Absi, Mechanistic Understanding of the Adsorption and Thermodynamic Aspects of Cationic Methylene Blue Dye onto Cellulosic Olive Stones Biomass from Wastewater, *Sci. Rep.*, 2020, **10**, 15928, DOI: 10.1038/s41598-020-72824-8.

75 J. Yang and K. Qiu, Preparation of Activated Carbons from Walnut Shells via Vacuum Chemical Activation and Their Application for Methylene Blue Removal, *Chem. Eng. J.*, 2010, **165**(1), 209–217, DOI: 10.1016/j.cej.2010.09.021.

76 I. A. W. Tan, A. L. Ahmad and B. H. Hameed, Adsorption of Basic Dye Using Activated Carbon Prepared from Oil Palm Shell: Batch and Fixed Bed Studies, *Desalination*, 2008, **225**(1–3), 13–28, DOI: 10.1016/j.desal.2007.04.031.

77 G. McKay, J. F. Porter and G. R. Prasad, The Removal of Dye Colours from Aqueous Solutions by Adsorption on Low-Cost Materials, *Water Air Soil Pollut.*, 1999, **114**(3–4), 423–438, DOI: 10.1023/A:1005191529836.

78 A. Salama and P. Hesemann, Guanylated Chitosan Derivatives for the Adsorption of Anionic Dyes: Performance and Mechanism, *Int. J. Biol. Macromol.*, 2025, **311**, 143852, DOI: 10.1016/j.ijbiomac.2025.143852.

79 E. E. P. Setyawati, J.-W. Zhang, N. D. Hai, M. A. l Kholif, M. R. Bilad and H.-P. Chao, Development of Composites from Titanate Nanotubes, Layered Double Hydroxides, and Oyster Shells for the Enhanced Removal of Methylene Blue, Acid Red 1, and Congo Red from Aqueous Solutions, *Adsorption*, 2025, **31**, 6, DOI: 10.1007/s10450-024-00689-8.

80 Y. You, L. Liu and G. Wu, Efficient Removal of Methylene Blue by Sodium Alginate–Carboxymethyl Cellulose–Kaolin Composite Microbeads, *J. Appl. Polym. Sci.*, 2025, **142**(15), 56993, DOI: 10.1002/app.56993.

81 M. Alomar, A. A. Khan and M. Yar, DFT Investigation of Co/Ni Decorated Borophene for Efficient Removal of Methylene Blue from Wastewater Effluent, *J. Mol. Liq.*, 2025, **417**, 126627, DOI: 10.1016/j.molliq.2025.126627.

82 BIOVIA, D. S., Forcite Code, Dassault Systèmes, San Diego, CA, USA, 2023.

83 N. U. Rahman, A. A. Khan, R. Ullah, R. Ahmad and I. Ahmad, Selective Sensing of NH3 and CH2O Molecules by Novel 2D Porous Hexagonal Boron Oxide (B3O3) Monolayer: A DFT Approach, *Surf. Interfaces*, 2022, **29**, 101767, DOI: 10.1016/j.surfin.2022.101767.